Surface & Coatings Technology 516 (2025) 132774

Contents lists available at ScienceDirect

Surface & Coatings Technology

journal homepage: www.elsevier.com/locate/surfcoat

Performance evaluation of TiAlSiN and TiSiN/TiSiVN coatings during high-speed dry turning of AISI 316 L considering the role of vanadium-based tribo-oxides☆

Ch. Sateesh Kumar [a,b], Luis Norberto López de Lacalle [c,d,*], Albano Cavaleiro [b], Diogo Cavaleiro [b], Mitjan Kalin [a], Ramanand Prajapati [e,g], Filipe Fernandes [b,f]

[a] Laboratory for tribology and interface nanotechnology, Faculty of Mechanical Engineering, University of Ljubljana, Askerceva 6, 1000, Ljubljana, Slovenia
[b] University of Coimbra, CEMMPRE, ARISE, Department of Mechanical Engineering, Rua Luís Reis Santos, 3030-788, Coimbra, Portugal
[c] CFAA- Aeronautics Advanced Manufacturing Centre, University of the Basque Country (UPV/EHU), Biscay Science and Technology Park, Ed. 202, Zamudio, Spain
[d] Department of Mechanical Engineering, University of the Basque Country, Escuela Superior de Ingenieros Alameda de Urquijo S/N, 48013, Bilbao, Spain
[e] Department of Mechanical Engineering, Indian Institute of Technology, Bhilai, India
[f] ISEP, Polytechnic of Porto, Rua Dr. António Bernardino de Almeida, 4249-015, Porto, Portugal
[g] Shri Shankracharya Technical Campus, Bhilai, India

ARTICLE INFO

Keywords:
TiSiN/TiSiVN coating
dry turning
self-lubricant coating
tool wear
AISI 316 L

ABSTRACT

This study investigates the tribo-mechanical performance of uncoated, TiAlSiN-coated, and TiSiN/TiSiVN multilayer-coated Al_2O_3/SiC ceramic tools during dry turning of AISI 316 L austenitic steel across three successive passes at varying cutting speeds. Key machining outputs, including cutting forces, surface roughness, cutting temperature, and tool wear (flank and crater), were analyzed with a focus on oxide formation and self-lubricating mechanisms. The TiSiN/TiSiVN-coated tool exhibited the most favorable performance, showing only ~15 % increase in cutting force across passes, ~9 % improvement in flank wear resistance compared to TiAlSiN, and ~ 17 % lower wear progression relative to the uncoated tool at 350 m/min. Surface roughness and cutting temperature trends further confirmed the coating's superiority, attributed to the formation of V_2O_5 tribo-oxides, which reduce friction and thermal degradation. EDS and SEM analyses validated the wear protection mechanisms, highlighting the adaptive role of vanadium-based layers in mitigating adhesion and thermal fatigue. The results establish TiSiN/TiSiVN as a promising candidate for high-speed dry machining due to its superior mechanical-chemical synergy and wear resistance.

1. Introduction

The development of advanced engineering materials—particularly austenitic stainless steels like AISI 316 L—now presents many difficulties for contemporary machining operations. Thanks in great part to its exceptional strength, biocompatibility, and corrosion resistance, AISI 316 L finds great application in the biomedical, petrochemical, and marine industries. But especially in dry conditions, its low heat conductivity, great strain hardening capacity, and adhesive wear tendency make machining quite challenging [1–4]. In dry turning applications, these characteristics result in high cutting forces, severe tool wear, undesired chip shape, and surface degradation; hence, the development of sophisticated tool materials and surface treatments able to withstand such tribo-mechanical loads [5–8].

Although cutting fluid removal strains the tool-workpiece interface even more, it is preferred from an environmental and financial standpoint. Accelerated oxidation, thermal softening, plastic deformation, and mechanical chipping of standard tools are brought about by high interface temperatures and frictional loads. Using cutting tools with advanced thin films in dry machining helps to increase cutting performance and tool lifetime. Under challenging tribological conditions, these coatings are supposed to have low friction, great hardness, chemical inertness, and thermal insulation [9–14].

Among the coatings investigated for dry machining, TiAlSiN has

☆ This article is part of a Special issue entitled: 'Functional Coatings: From Lab to Applications' published in Surface & Coatings Technology.

* Corresponding author at: CFAA- Aeronautics Advanced Manufacturing Centre, University of the Basque Country (UPV/EHU), Biscay Science and Technology Park, Ed. 202, Zamudio, Spain.
E-mail address: norberto.lzlacalle@ehu.eus (L.N. López de Lacalle).

https://doi.org/10.1016/j.surfcoat.2025.132774
Received 16 July 2025; Received in revised form 15 September 2025; Accepted 7 October 2025
Available online 8 October 2025

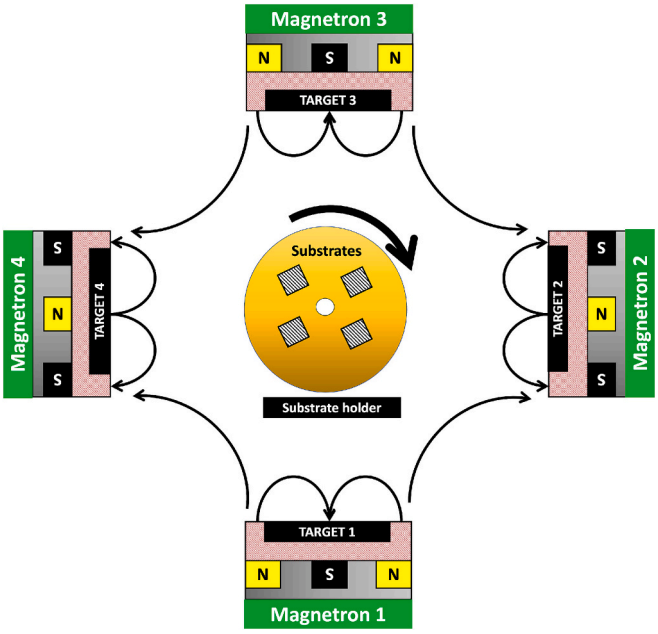

Fig. 1. Schematic representation of DC reactive magnetron sputtering setup

gained significant attention due to its nanocomposite microstructure and excellent thermal stability. It typically consists of crystalline TiN grains embedded within an amorphous Si_3N_4 and AlN matrix [15,16]. This configuration enhances the coating's hardness, fracture toughness, and oxidation resistance. During high-temperature operation, Al in the coating oxidizes to form dense Al_2O_3 films, acting as protective diffusion barriers that minimize substrate oxidation and thermal degradation [17]. Additionally, the amorphous Si_3N_4 phase refines grain structure and contributes to hardness via grain boundary strengthening [18–20]. The fine columnar architecture of TiAlSiN, developed during PVD growth, contributes to its superior resistance against abrasive and adhesive wear [21].

Despite these advantages, TiAlSiN mostly provides passive protection using the stability of oxide films. The coating cannot dynamically adjust to changing tribo-chemical conditions in extended dry cutting conditions including cyclic thermal and mechanical loads. TiSiN-based nanocomposites—in which TiN nanocrystals are arranged over an amorphous Si_3N_4 matrix—have been investigated. Stable microstructure and amorphous network of TiSiN provide amazing resistance to thermal softening and hardness. Its low thermal diffusivity slows heat penetration into the tool substrate, so enhancing performance in high-speed, high-load applications [22–24].

Furthermore, limited by a lack of active self-lubricating ability are TiAlSiN and TiSiN. Adding vanadium to multilayer structures like TiSiN/TiSiVn is one fascinating way to get beyond this limitation. These coatings use the mechanical strength of TiSiN together with the self-adaptive tribo-chemical action of vanadium oxides. High cutting temperatures lead to oxidation of V atoms in the coating to generate low shear strength layered oxide V_2O_5 [25]. This oxide provides solid lubrication at the tool–chip interface, reducing the coefficient of friction and interface temperature while simultaneously delaying the onset of wear [26,27]. Alternating TiSiN and TiSiVN layers in the multilayered construction can also bring residual stress modulation depending on the interfaces. Acting as diffusers and crack arresters, these interfaces stop cracks from spreading, so enhancing toughness. Regular variations in the elastic modulus and hardness of the layers improve resistance to delamination and spalling even more [28]. Moreover, vanadium additions can alter oxidation kinetics, so favoring the generation of V_2O_5 over other non-lubricious oxides, such as Fe_2O_3, usually produced during stainless steel machining [29,30].

Combining passive (AlO_3, SiN_4) oxide generation with adaptive (V_2O_5) oxide generation in TiSiN/TiSiVN coatings can provide a dual-mode protection mechanism. While passive oxides serve as chemical and thermal barriers, the adaptive V_2O_5 layer dynamically reacts to temperature rises by generating low-friction interfaces. All around the tool life, this improves surface quality, chip evacuation, and tribological stability. Recent research shows that coatings with vanadium content lower wear and enhance tool life during adverse machining conditions [27,31]. While these coating systems have promise, most evaluations of them depend on single-pass turning tests or interrupted machining, which cannot reasonably replicate cutting conditions in the real world. Tools in real-world manufacturing settings run for long periods of time and suffer cumulative damage from adhesion, chip load, and repeated heat cycles. Single-pass studies [32–35] neglect the dynamic evolution of wear mechanisms, oxide film generation, and chemical transformation in the cutting zone.

Thus, the present work investigates the performance of TiAlSiN and TiSiN/TiSiVN coatings on Al_2O_3/SiC cutting tools during dry turning of 316 L austenitic steel. The machining would be conducted in a three-pass setup so as to better understand the variation of output parameters with cutting speed over a range of cutting lengths. Following each pass, parameters including temperature, crater and flank wear, cutting force, surface roughness, and coefficient of friction are measured.

2. Experimental methodology

2.1. Coating deposition

The TiAlSiN monolayer and TiSiN/TiSiVN multilayer coatings were deposited in a semi-industrial TEER sputtering machine, using DC reactive magnetron sputtering. The process begins with substrate preparation, where cemented carbide cutting tools were ultrasonically cleaned in acetone and ethanol to remove contaminants, dried using nitrogen gas, and mounted inside the vacuum chamber. The substrates underwent argon plasma etching before deposition to enhance adhesion by eliminating oxides and impurities. Then, the sputtering chamber was evacuated to a base pressure of approximately 9.0×10^{-4} Pa, followed by the introduction of high-purity argon (Ar) and nitrogen (N_2) gases as the working and reactive gases. The chamber has 4 magnetrons, evenly distributed on the chamber diameter, i.e. making 90° between each target. The size of each of the targets was 380 mm × 175 mm × 10 mm, and the distance between the targets and the substrate was 150 mm. To produce the TiAlSiN coating, independent high purity (99.9 % purity) Ti, Al and Si targets were used in the deposition. The power applied to the targets was 2500 W, 2000 W and 600 W for Ti, Al and Si targets, respectively. The multilayer TiSiN/TiSiVN was produced in the same chamber using individual Ti (2500 W), Si (600 W) and V(1800 W). To produce the multilayer, the V target was turned on and turned off every 5 min. The substrates were etched using Ar ion sputtering at 600 V and 250 kHz in a DC-pulsed power supply for 40 min. To enhance film adhesion to the substrate, a Cr interlayer and a CrN gradient layer were deposited from a Cr target. The Cr interlayer was produced using 35 sccm of Ar while applying 2000 W for 10 min. The gradient layer with increasing N content was produced by maintaining an Ar flow of 35 sccm, applying 2000 W to the Cr target, and gradually increasing the nitrogen flow up to 18 sccm over 10 min. A second gradient layer, formed by progressively decreasing the power applied to the Cr target while simultaneously increasing the power applied to the Ti, Al and Si targets or Ti Si V targets (for TiAlSiN ot TiSiN/TiSiVN coatings), until reaching the desired power value. All depositions were carried out with an argon flow of 40 sccm and a nitrogen flow of 18 sccm with the powers applied to the different targets. The substrate holder was rotated at 10.5 rpm. A pulsed negative bias of 50 V (250 kHz) was applied to the substrate holder during the deposition of the final layers. Fig. 1 shows the schematic representation of the coating deposition setup.

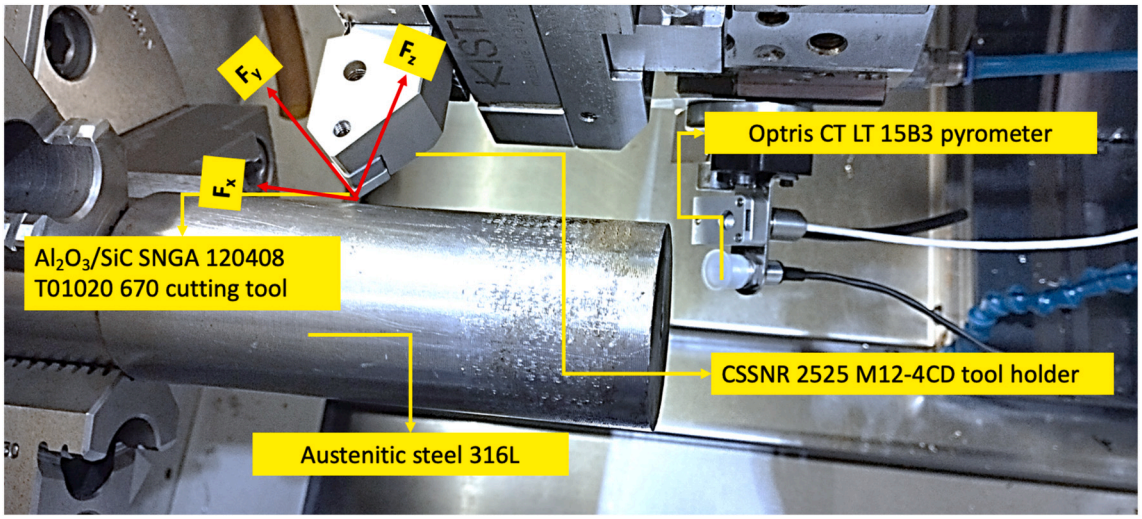

Fig. 2. Turning tests experimental setup.

Table 1
Machining parameters for turning tests.

Tool material	Al_2O_3/SiC whiskers reinforced ceramic
Workpiece material	316 L austenitic steel
Coatings	Monlayered-TiAlSiN, multilayered-TiSiN/TiSiVN
Tool holder	CSSNR 2525 M12–4CD
Cutting insert designation	SNGN 120408 T01020
Cutting speeds (m/min)	200, 250, 300, 350
Depth of cut (mm)	0.5
Feed rate (mm/rev)	0.1
Cutting length for each pass (mm)	100
Number of passes	3

Table 2
Chemical composition, hardness, and Young's modulus of the coatings.

Coating	Chemical composition (at. %)	Hardness and Young's modulus
TiAlSiN	N - 47.5 Ti - 29.1 Si - 10.1 Al - 13.3	H – 19 ± 1 GPa E – 280 ± 13 GPa
TiSiN/TiSiVN	N - 52.1 Ti - 27.7 Si - 14.2 V - 6.1	H – 21 ± 1 GPa E – 235 ± 7 GPa

2.2. Turning tests

The turning tests were carried out under dry machining conditions to evaluate the performance of Al_2O_3/SiC ceramic inserts with three configurations: uncoated, TiAlSiN-coated, and TiSiN/TiSiVN multilayer-coated Al_2O_3/SiC whiskers reinforced cutting tools. The primary objective was to assess the evolution of machining forces, surface integrity, cutting temperature, and wear mechanisms during high-speed dry turning of AISI 316 L austenitic stainless steel. The experimental setup in shown in Fig. 2.

Machining forces were measured using a triaxial Kistler piezoelectric dynamometer, enabling the acquisition of tangential, radial, and axial components of force. Each force measurement was recorded in real time and synchronized with cutting speed variations ranging from 200 to 350 m/min. The detailed machining parameters are listed in Table 1. The measured machining forces were used to calculate the coefficient of friction (μ_{ap}) as per the equation below.

$$\mu_{ap} = \frac{F_{XZ} + F_Y tan\propto}{F_Y - F_{XZ} tan\propto} \quad (1)$$

$$F_{XZ} = \sqrt{{F_X}^2 + {F_Y}^2} \quad (2)$$

where F_Y = Cutting force
F_X = Feed force
F_Z = Thrust force
F_{XZ} = Equivalent thrust force
and $\propto$ = Orthogonal rake angle (-8^o)

The cutting temperature was continuously monitored using a CT LT 15B3 non-contact infrared pyrometer aimed directly at the tool–chip interface. Temperature readings were averaged over the entire cutting length to minimize transient effects. Surface integrity was evaluated by measuring the average surface roughness (R_A) of the machined workpieces using a Taylor Hobson contact-type stylus profilometer. For statistical robustness, R_A was measured five times per pass on each machined sample and averaged. To ensure experimental reliability, each machining condition was repeated three times, and all measured responses, including forces, temperature, roughness, and wear, were averaged across the three repetitions, with associated error bars computed and reported. Flank and crater wear were analyzed using scanning electron microscopy (SEM) and energy-dispersive X-ray spectroscopy (EDS) to determine the dominant wear mechanisms and elemental migration patterns in the worn zones. FESEM (Zeiss, Gemini 500) was operated at 5–15 kV with a working distance of 8–10 mm. Elemental analyses were carried out with an SDD detector (129 eV resolution). To distinguish O and V, low-kV (7–10 kV) maps were used for oxygen, while V was confirmed through its Kα peak (~4.95 keV) at 15–20 kV. Raman analysis was performed at the chip-tool interface of the coated tools so as to better understand the formation of different oxides. Raman spectra were recorded using a *Renishaw inVia Raman microscope* with a 532 nm laser (power 0.6–1 mW at the sample, 50× objective, ~1–2 μm spot). Each spectrum was collected with 10 s integration and 3 accumulations, with a spectral resolution of ~2 cm^{-1}.

3. Results and discussion

3.1. Coatings chemical composition, mechanical properties, morphology and structure

The chemical composition of the coatings and their mechanical properties are presented in Table 2. Both coatings displayed a near

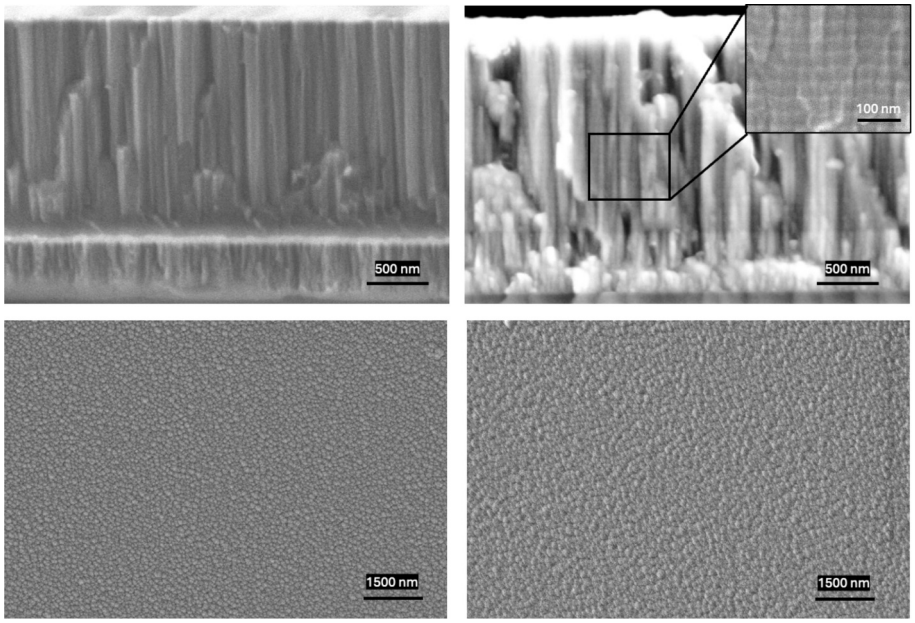

Fig. 3. Cross section and surface morphology of: a) and b) TiAlSiN film, c) and d) TiSiN/TiSiVN film obtained in SE mode.

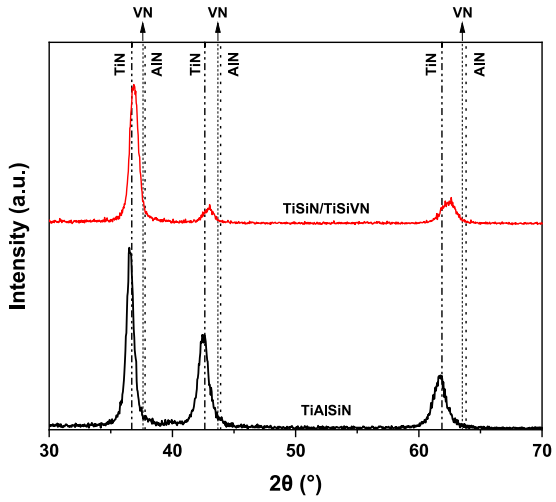

Fig. 4. XRD diffraction patterns of the films. The following ICDD reference cards were included: TiN 87–0633, AlN 25–1495 and VN 35–0768.

stoichiometric composition with the N concentration close to 50 at.%. The hardness values are also very similar; however, the Young's modulus is higher for the TiAlSiN coating as a result of the more compact morphology, leading to a lower bonding energy between elements.

Both films exhibit a typical columnar morphology, with columns extending from the interlayer/gradient layer to the coating surface (see Fig. 3). The TiAlSiN film shows a slightly more compact morphology than the TiSiN/TiSiVN film, consistent with the smaller surface features corresponding to the column terminations. This higher compactness in the TiAlSiN film is likely due to the higher global power applied to the targets, which increases the sputtering yield and, consequently, the flux of adatoms arriving at the growing film. The higher adatom flux promotes additional nucleation sites, resulting in a denser and more compact morphology. In both coatings, the interlayer used to improve adhesion can be seen at the bottom. Additionally, in the TiSiN/TiSiVN film a multilayer altering TiSiN (lighter layer) and TiSiVN (dark layer) layer with a period thickness of 52 nm can be observed.

Fig. 4 presents the XRD diffraction patterns of the as-deposited coatings obtained in conventional mode. As expected, both coatings exhibit several intense peaks belonging to the (111), (200) and (220) diffraction plans of an fcc-type structure. Al should occupy substitutional positions in the fcc structure. This corroborates the results from the literature, where Ti1-xAlxN coatings with a NaCl-type structure were always produced for an aluminium concentration inferior to 35 at. % [36]. Si element should also be positioned on solid solution in the fcc structure and form amorphous SiNx phase, to produce a nc-TiAlN/a-SiN4x nanocomposite structure, as reported in the literature [37]. This nanocomposite configuration normally promotes grain refinement and contributes to higher hardness and Young's modulus. Diffraction peaks of multilayer TiSiN/TiSiVN film are shifted to higher angle values as compared to TiAlSiN film. This may be explained by the presence of Si in solid solution, which, due to its lower atomic radius as compared to Al, shifts the diffraction peaks to higher diffraction angles. The different levels of compressive residual stresses taking place on the films (not measured in this work) also influence the position of the XRD diffraction peaks. Despite of the presence of Si in solid solution formation of amorphas SiNx is also expected [38]. V should occupy substitutional positions on the fcc lattice as reported in the literature. Finally, although a multilayer structure was grown, all the fcc diffraction peaks for the multilayer structure correspond to a cumulative signal from the individual layers of the multi-layered structure with different chemical composition, TiSiN and TiSiVN. This contributes to the broadening of the width of the XRD diffraction peaks, determined by the existence of different lattice parameters, from TiSiN and TiSiVN layers. The deconvolution of the XRD peaks is not easy to perform due to the expected small variation in the lattice parameters of layers in a multilayer structure.

3.2. Machining forces

The variation in cutting force (F_Y) over three successive passes for uncoated, TiAlSiN-coated, and TiSiN/TiSiVN-coated tools at different cutting speeds is illustrated in Fig. 5(a–d). Cutting forces progressively increased with both speed and number of passes for all tools, a trend that reflects the cumulative influence of thermal loading, tool wear, and friction at the tool–chip interface during dry turning of AISI 316 L stainless steel. For the uncoated tool, the most aggressive increase in F_Y was observed. Between the first and third pass, the cutting force

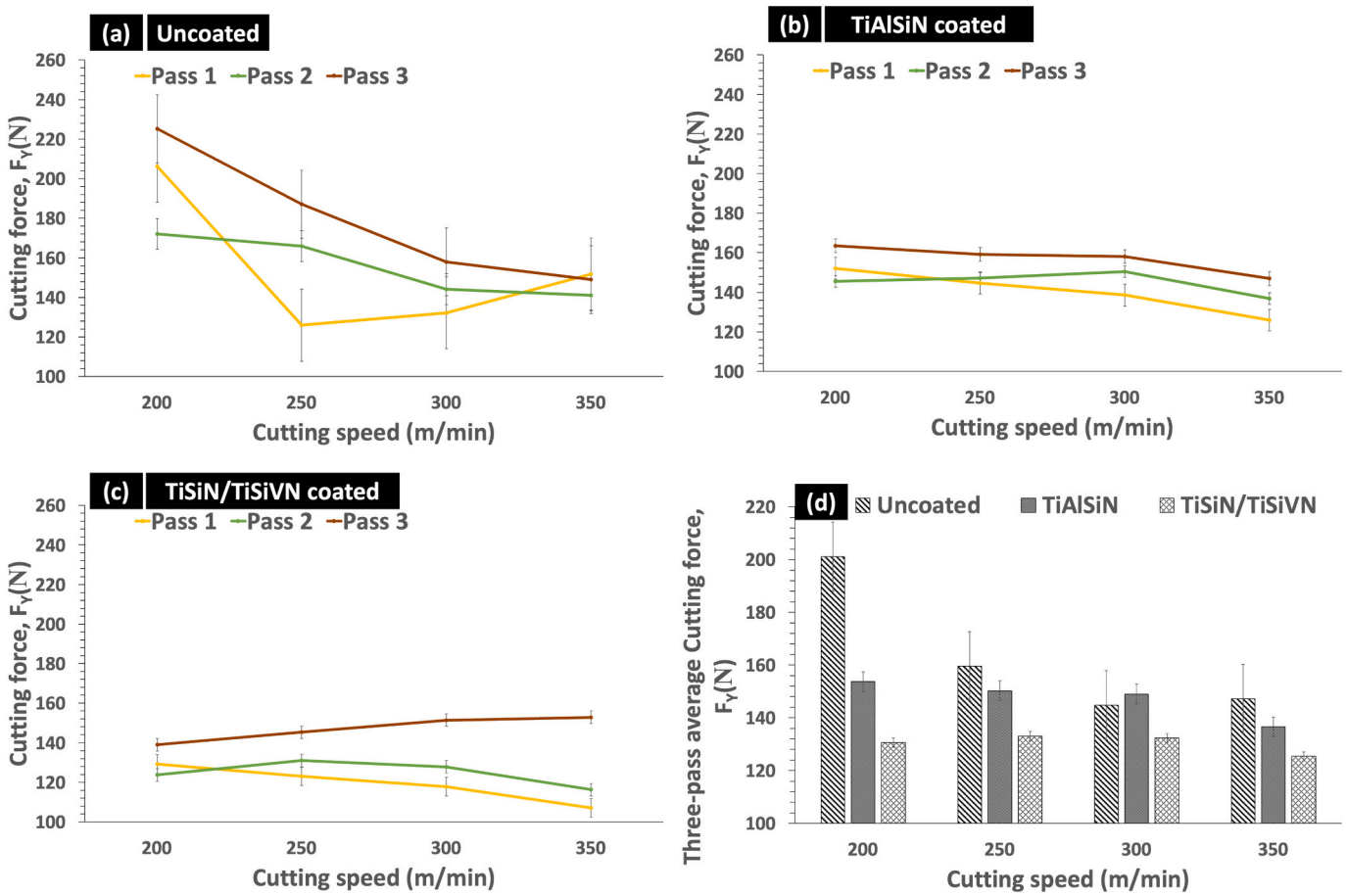

Fig. 5. Variation of cutting force, $F_{Y,}$ with cutting speed and subsequent passes for (a) Uncoated, (b) TiAlSiN coated, and (c) TiSiN/TiSiVN coated tools and (d) three-pass average cutting force variation with cutting speed for coated and uncoated cutting tools.

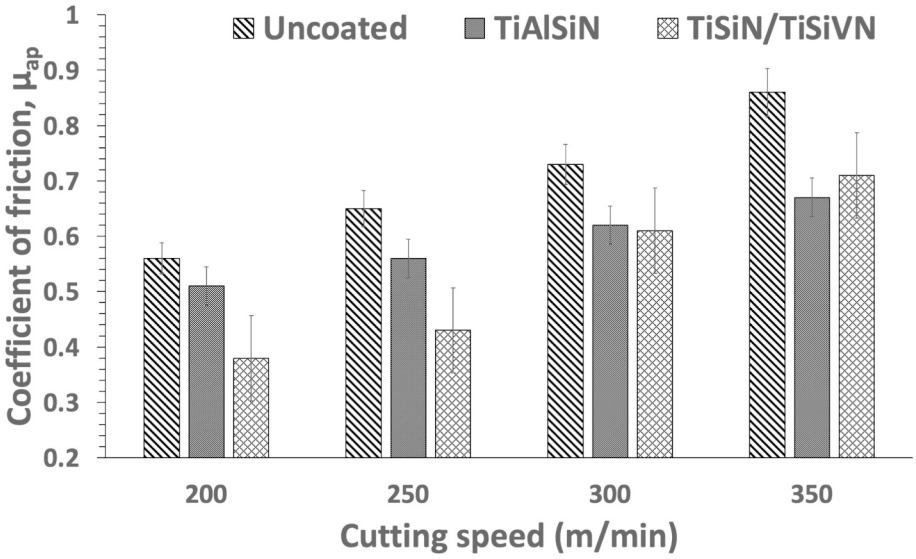

Fig. 6. Variation of coefficient of friction with cutting speed for different cutting tools.

increased by approximately 23 % at 200 m/min, 27 % at 250 m/min, 30 % at 300 m/min, and 32 % at 350 m/min. This sharp rise corresponds to adhesive wear, thermal degradation, and rapid tool edge deformation in the absence of any tribological protection at elevated temperatures. Similar patterns of cutting force escalation in uncoated ceramics during stainless steel machining have been reported by Ginting and Nouari [39].

The TiAlSiN-coated tool showed improved force behavior compared to the uncoated tool. The force increase between passes was more gradual: approximately 18 % at 200 m/min, 22 % at 250 m/min, 25 % at 300 m/min, and 28 % at 350 m/min. The enhanced thermal stability of TiAlSiN, attributed to the formation of dense Al_2O_3 scales, slows the rate

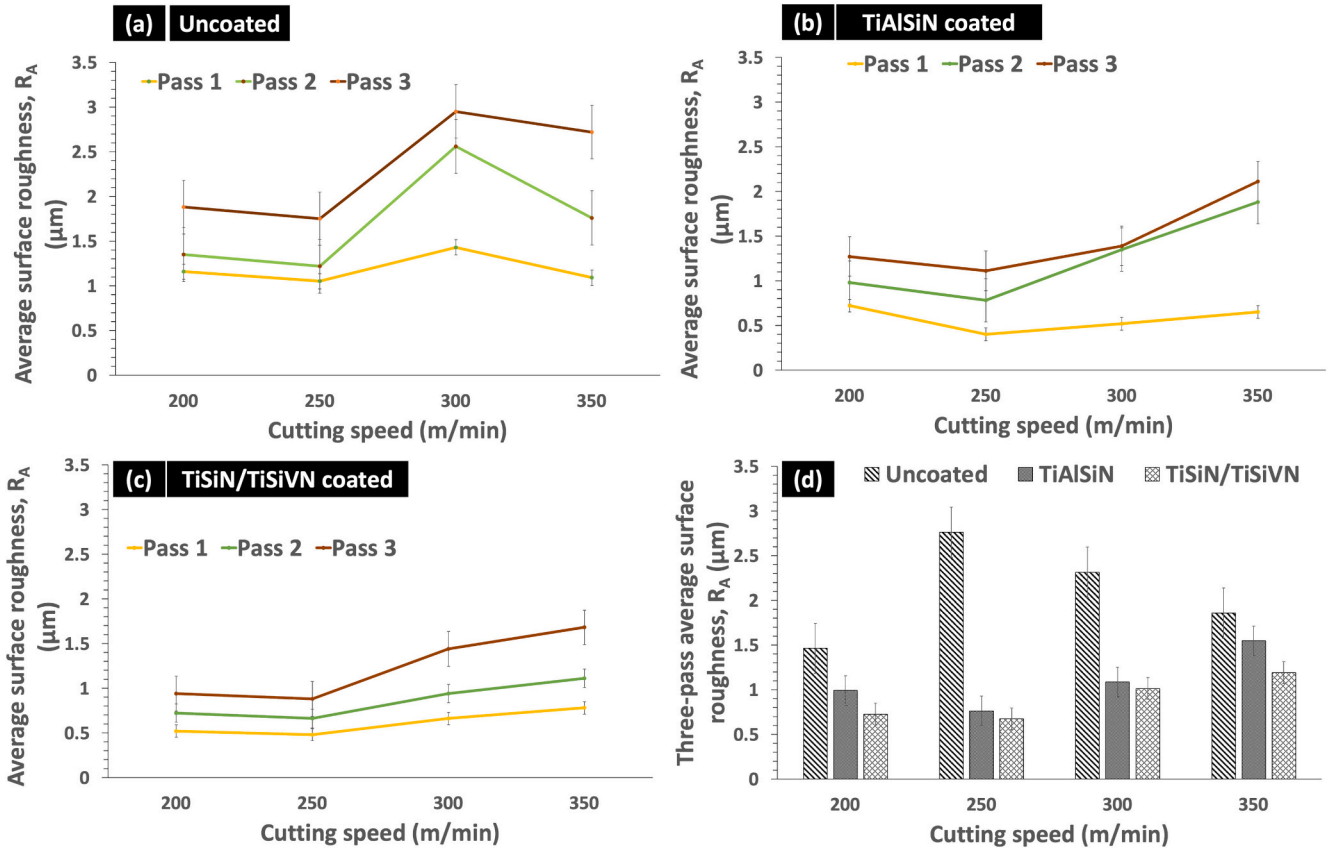

Fig. 7. Variation of average surface roughness, R_A, with cutting speed and subsequent passes for (a) Uncoated, (b) TiAlSiN coated, and (c) TiSiN/TiSiVN coated tools and (d) three-pass average surface roughness variation with cutting speed for coated and uncoated cutting tools.

of thermal wear. However, TiAlSiN coatings rely on passive oxide protection and lack the capability to actively reduce friction, limiting their performance during extended dry cutting. In contrast, the TiSiN/TiSiVN-coated tool exhibited the lowest and most stable cutting force profile across all speeds. The pass-to-pass increase in F_Y was only 12–15 %, significantly lower than for the other tools.

A direct comparison of average F_Y across all passes (Fig. 5d) revealed that at 200 m/min, TiSiN/TiSiVN lowered the average cutting force by ~18 % compared to the uncoated tool and ~ 11 % compared to TiAlSiN. These reductions remained consistent even at 300 m/min, with FY drops of ~16 % and ~ 10 %, respectively. At 350 m/min, the TiSiN/TiSiVN tool continued to maintain its advantage, reducing average F_Y by ~17 % relative to the uncoated tool and ~ 9 % compared to TiAlSiN. In essence, the TiSiN/TiSiVN-coated tool outperforms both TiAlSiN and uncoated ceramics by effectively combining passive oxide stability (from Si_3N_4 and TiN) with adaptive tribo-chemical lubrication via V_2O_5 formation. This dual mechanism minimizes mechanical resistance, delays thermal softening, and preserves edge geometry—critical factors for maintaining low cutting forces under lubricant-free conditions [25,40].

3.3. Coefficient of friction

The variation in average coefficient of friction (COF) over three passes at different cutting speeds is presented in Fig. 6. Across all speeds, a general trend of increasing frictional behavior was observed, with distinct differences in performance among the tool systems. These trends show a strong correlation with the machining force behavior discussed earlier, as both COF and cutting forces are influenced by interfacial contact, adhesion, and thermal load. For the uncoated tool, COF increased by approximately 20 % from 200 m/min to 350 m/min. This rise is attributed to the accumulation of adhered material at the tool–chip interface, increased tool-workpiece contact area due to progressive wear, and the absence of any protective oxide layer. This also aligns with the observed rise in cutting forces for the uncoated tool, which experienced a similar percentage increase due to escalating chip-tool friction and tool edge deformation.

The TiAlSiN-coated tool showed a more moderate increase of approximately 17 % in COF across the same speed range. In contrast, the TiSiN/TiSiVN-coated tool demonstrated the lowest overall friction and the smallest increase, only about 13 % from 200 m/min to 350 m/min. The relatively stable COF progression correlates well with the cutting force trends for this coating, which also exhibited the least percentage increase in forces (~15 %) over the passes.

The lower rate of increase in COF for the TiSiN/TiSiVN tool highlights its superior friction-regulating ability under dry machining conditions. This tribological advantage directly contributes to reduced force generation, lower tool temperature, and improved surface finish, as corroborated by the temperature and roughness results. In essence, the coefficient of friction data not only reflects surface interactions but also reinforces the tool's ability to maintain mechanical stability over successive passes.

3.4. Surface roughness

The variation of average surface roughness (R_A) with cutting speed and tool condition across three successive passes is illustrated in Fig. 7 (a–d). Surface roughness increased steadily with both speed and number of passes for all tools, reflecting cumulative degradation in tool edge geometry, chip evacuation quality, and tribological contact under dry machining. For the uncoated tool (Fig. 7a), R_A values rose significantly, by approximately 38 % from pass 1 to pass 3 at 200 m/min, and by over 45 % at 300 m/min. These increases are indicative of edge chipping,

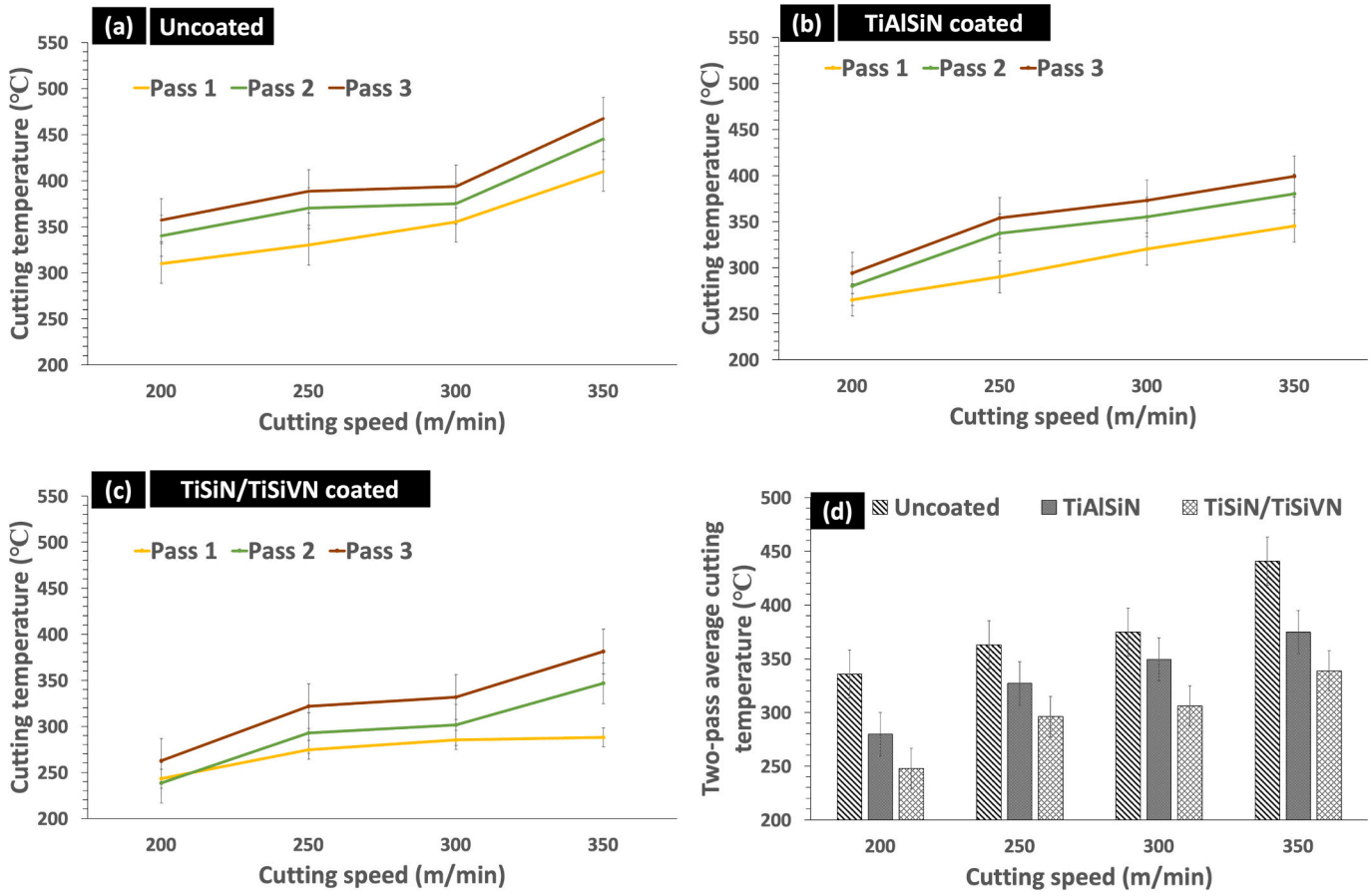

Fig. 8. Variation of cutting temperature cutting speed, and subsequent passes for (a) Uncoated, (b) TiAlSiN coated, and (c) TiSiN/TiSiVN coated tools and (d) three-pass average cutting temperature variation with cutting speed for coated and uncoated cutting tools.

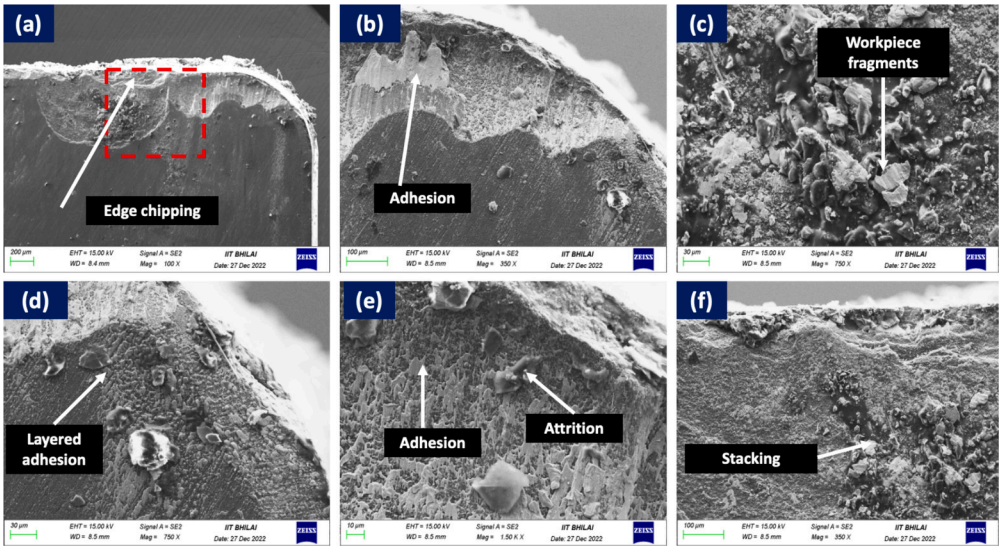

Fig. 9. SEM micrographs showing crater wear on the rake surface of uncoated Al_2O_3/SiC cutting tool.

flank wear, and work material adhesion at elevated temperatures, which are commonly observed in dry turning of austenitic stainless steels [41]. The surface quality deteriorated in parallel with cutting force escalation (~30 %) and friction increase (~20 %), underscoring the close correlation between interface mechanics and surface finish in the absence of lubrication.

The TiAlSiN-coated tool (Fig. 7b) showed relatively improved surface quality. Surface roughness increased by 28–32 % over passes, with average Ra values ~18 % lower than the uncoated tool at 300 m/min. However, since TiAlSiN does not possess self-lubricating capability, its surface finish still degraded with progressive thermal and mechanical loading, matching the increasing trend in COF and cutting forces observed earlier [20]. The TiSiN/TiSiVN-coated tool (Fig. 7c) delivered the best results in terms of surface quality. Surface roughness increased

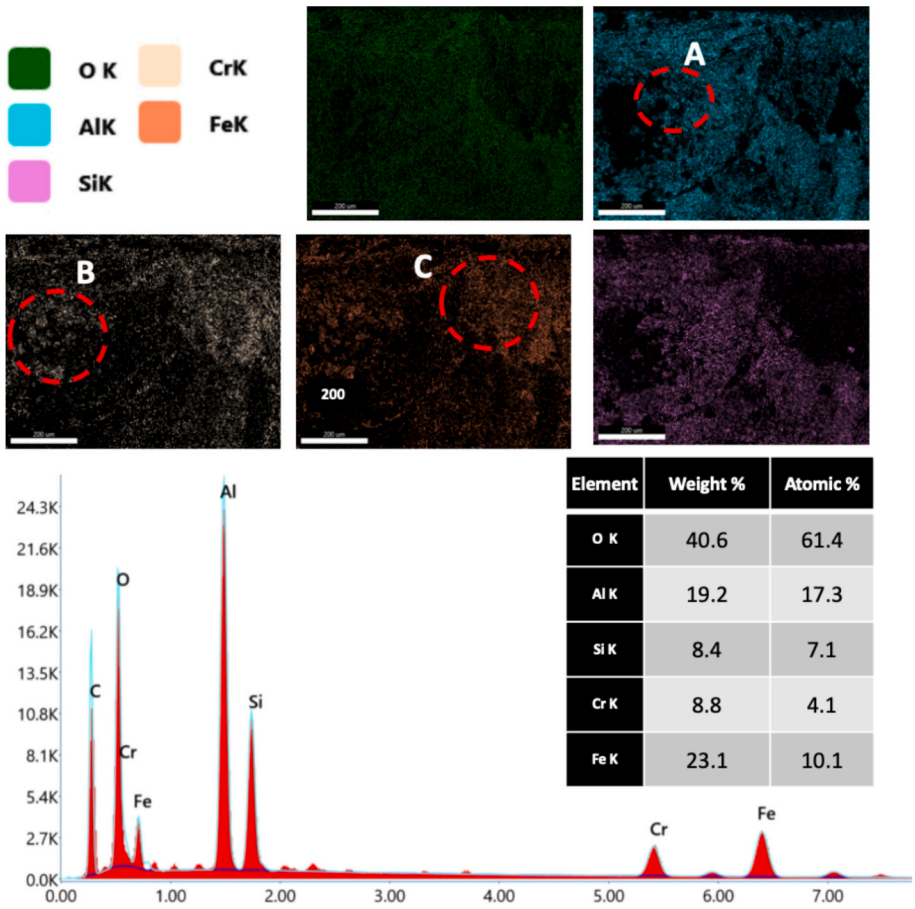

Element	Weight %	Atomic %
O K	40.6	61.4
Al K	19.2	17.3
Si K	8.4	7.1
Cr K	8.8	4.1
Fe K	23.1	10.1

Fig. 10. EDS elemental mapping of the marked region using the dashed red box in Fig. 7. (For interpretation of the references to colour in this figure legend, the reader is referred to the web version of this article.)

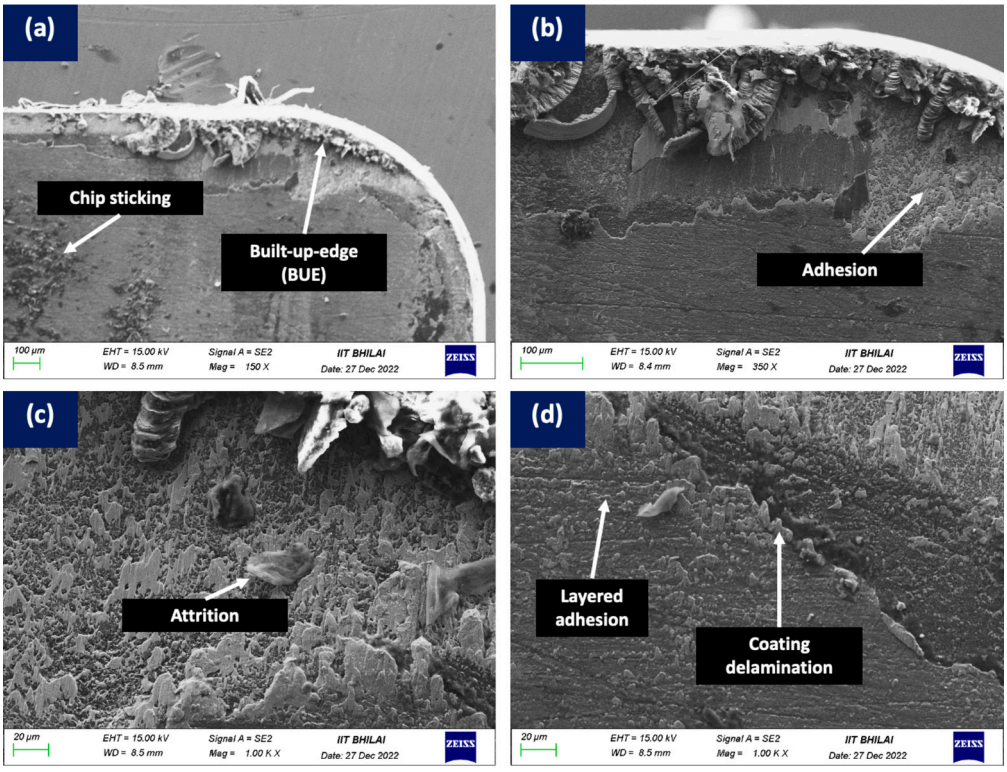

Fig. 11. SEM micrographs showing crater wear on the rake surface of uncoated Al_2O_3/SiC cutting tool.

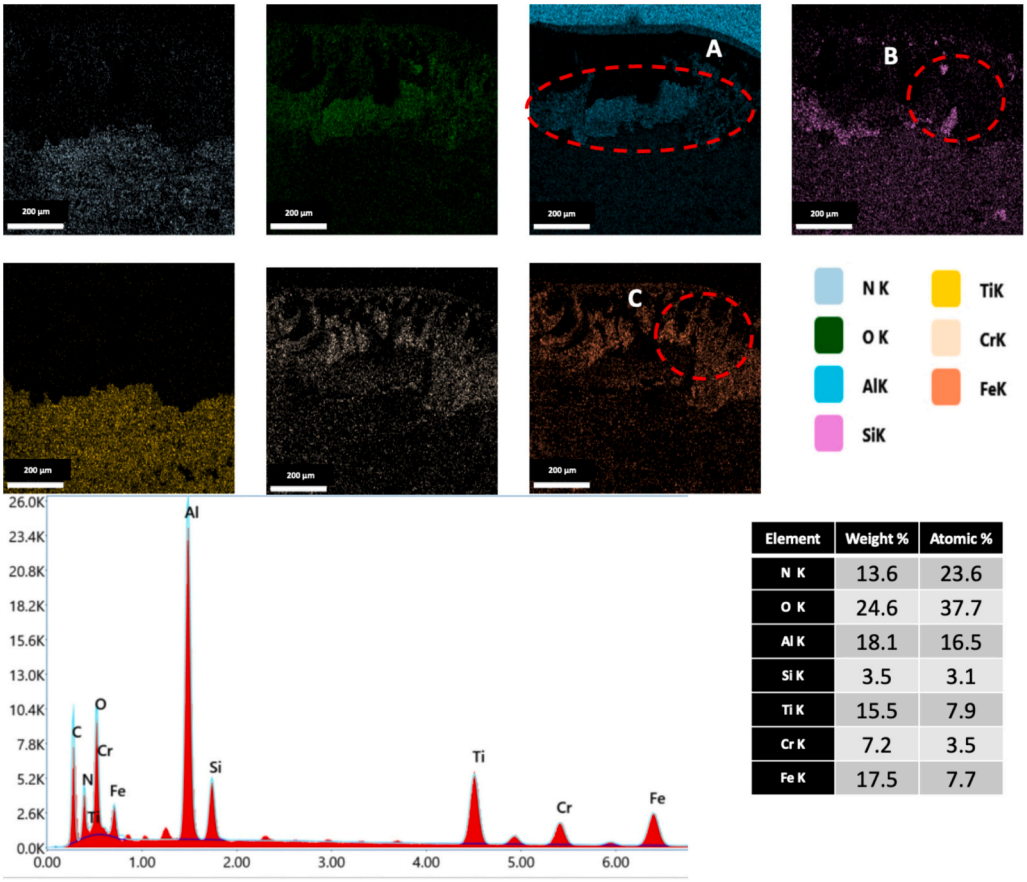

Element	Weight %	Atomic %
N K	13.6	23.6
O K	24.6	37.7
Al K	18.1	16.5
Si K	3.5	3.1
Ti K	15.5	7.9
Cr K	7.2	3.5
Fe K	17.5	7.7

Fig. 12. EDS elemental mapping of Fig. 9(b).

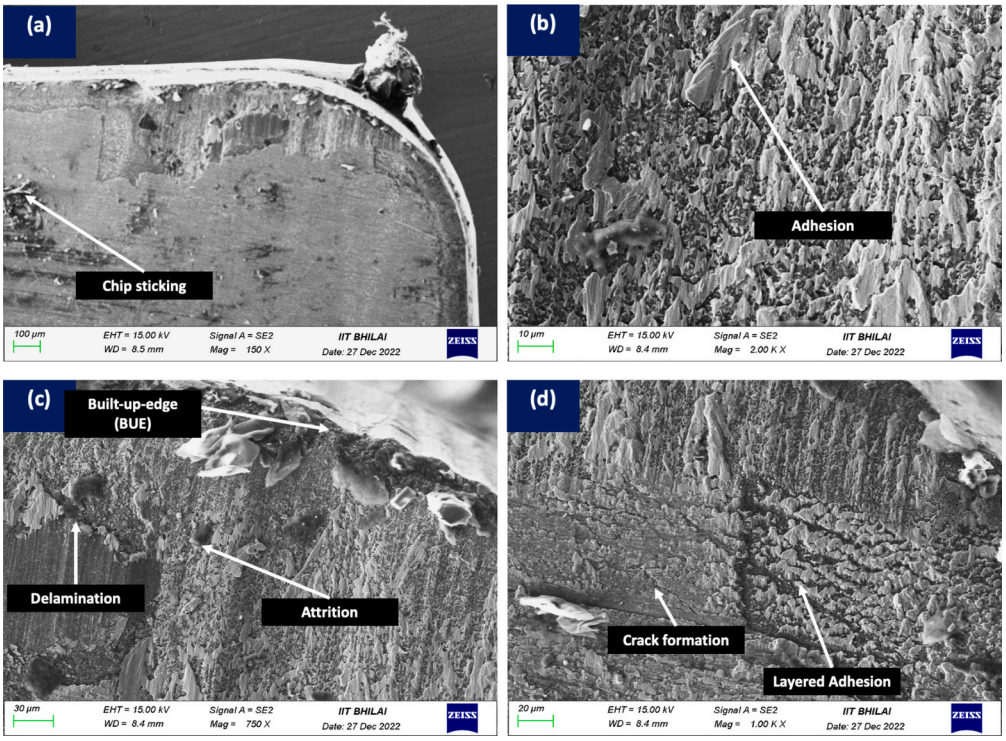

Fig. 13. SEM micrographs showing crater wear on the rake surface of TiSiN/TiSiVN coated Al_2O_3/SiC cutting tool.

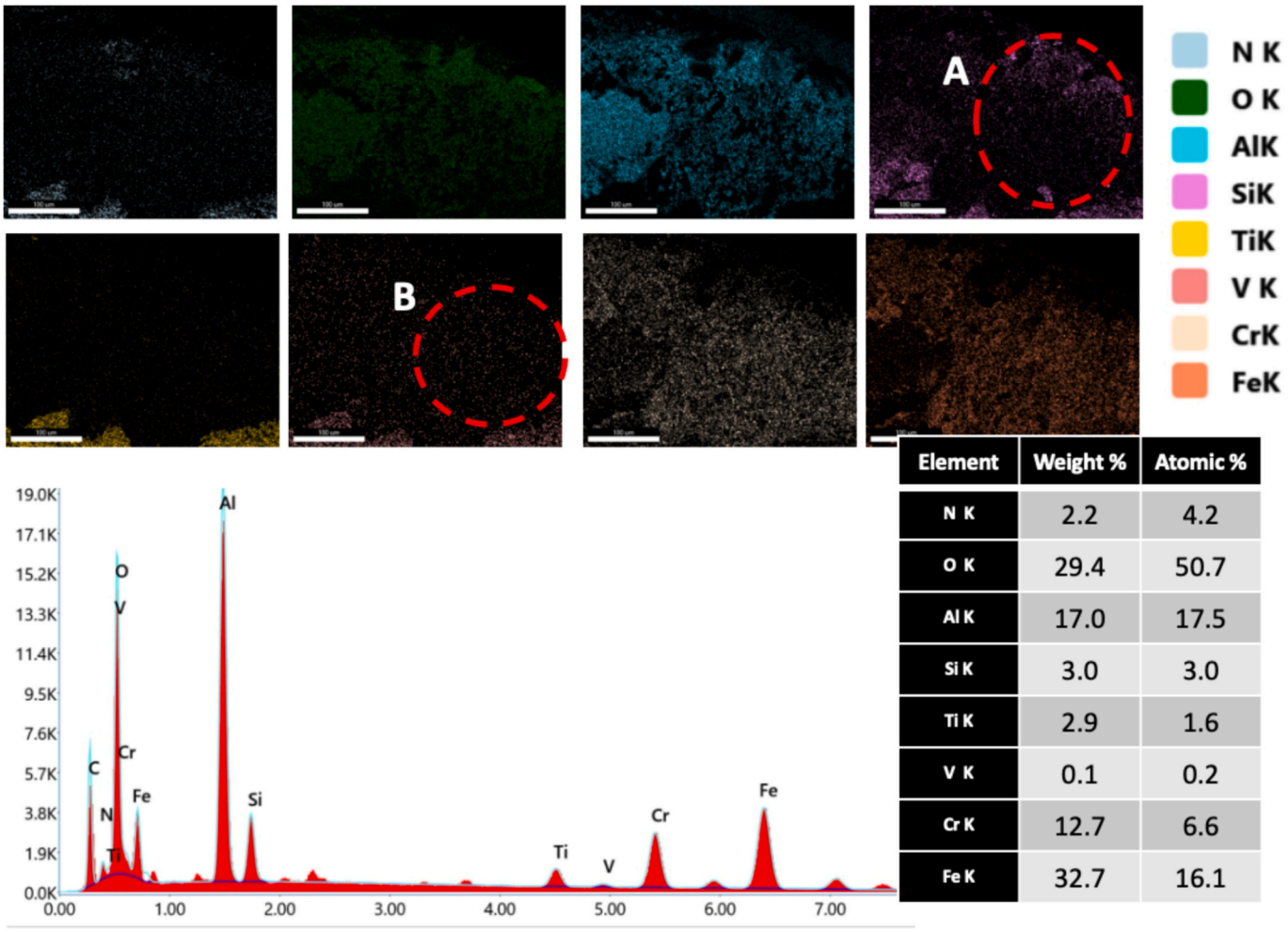

Element	Weight %	Atomic %
N K	2.2	4.2
O K	29.4	50.7
Al K	17.0	17.5
Si K	3.0	3.0
Ti K	2.9	1.6
V K	0.1	0.2
Cr K	12.7	6.6
Fe K	32.7	16.1

Fig. 14. EDS elemental mapping of Fig. 11(c).

by only 18–22 % with speed and passes, significantly less than for the other tools. As seen in Fig. 7d, R_a at 300 m/min was reduced by ~30 % compared to the uncoated tool and ~ 14 % compared to TiAlSiN. In summary, surface roughness trends mirror those of cutting force and COF, confirming the TiSiN/TiSiVN tool's ability to sustain topographic integrity under progressive wear and thermal cycling through its dual passive–adaptive oxide system.

3.5. Cutting temperature

The evolution of cutting temperature across three passes at various cutting speeds for different tool coatings is depicted in Fig. 8 (a–d). Temperature is a critical factor in dry machining, directly influencing friction, cutting force, and surface finish. As expected, cutting temperature increased with both cutting speed and number of passes due to cumulative thermal loading and progressive tool wear. For the uncoated tool (Fig. 8a), temperature showed the most aggressive rise. At 200 m/min, the average temperature increases from pass 1 to pass 3 was approximately 22 %, while at 300 m/min it rose by nearly 30 %. This escalation is primarily due to the absence of a thermal barrier layer, leading to rapid tool edge softening, increased adhesion, and severe material transfer—all of which accelerate wear and friction. The associated rise in COF (~20 %) and cutting force (~30 %) for this tool system is indicative of a deteriorating tool–chip interface and uncontrolled thermal feedback [41].

The TiAlSiN-coated tool (Fig. 8b) demonstrated improved thermal regulation. The temperature increase across passes was limited to 17–20 %. At 300 m/min, the average cutting temperature was reduced by ~10 % compared to the uncoated tool. This thermal control correlated with moderate gains in surface finish (Ra decreased by ~18 %) and restricted COF rise to about 17 %, confirming that TiAlSiN coatings resist heat-induced tool breakdown better than uncoated ceramics [18,42]. The TiSiN/TiSiVN-coated tool (Fig. 8c) exhibited the best thermal performance, with pass-to-pass temperature increases limited to 12–14 %. At 300 m/min, it maintained a temperature reduction of ~18 % compared to the uncoated tool and ~ 9 % relative to TiAlSiN. As a result, this tool exhibited the lowest average COF (~13 % increase), the most stable cutting force (~15 % increase), and the least surface roughness escalation (~20 % increase), confirming the synergistic thermal-frictional advantage of vanadium-based tribo-chemical adaptation [40]. The TiSiN/TiSiVN tool consistently provided better thermal control, leading to smoother cutting dynamics and improved workpiece surface quality.

3.6. Crater Wear – SEM and EDS analysis

Crater wear, located primarily on the rake face of the cutting tool, is a dominant wear mode in high-speed machining, particularly under dry conditions. It is often caused by thermal softening, adhesion, and chemical interaction between the tool and chip. Figs. 9 to 14 provide SEM micrographs and EDS elemental mappings of crater wear zones for the uncoated, TiAlSiN, and TiSiN/TiSiVN coated tools, enabling a detailed comparison of wear behavior, oxide formation, and material migration.

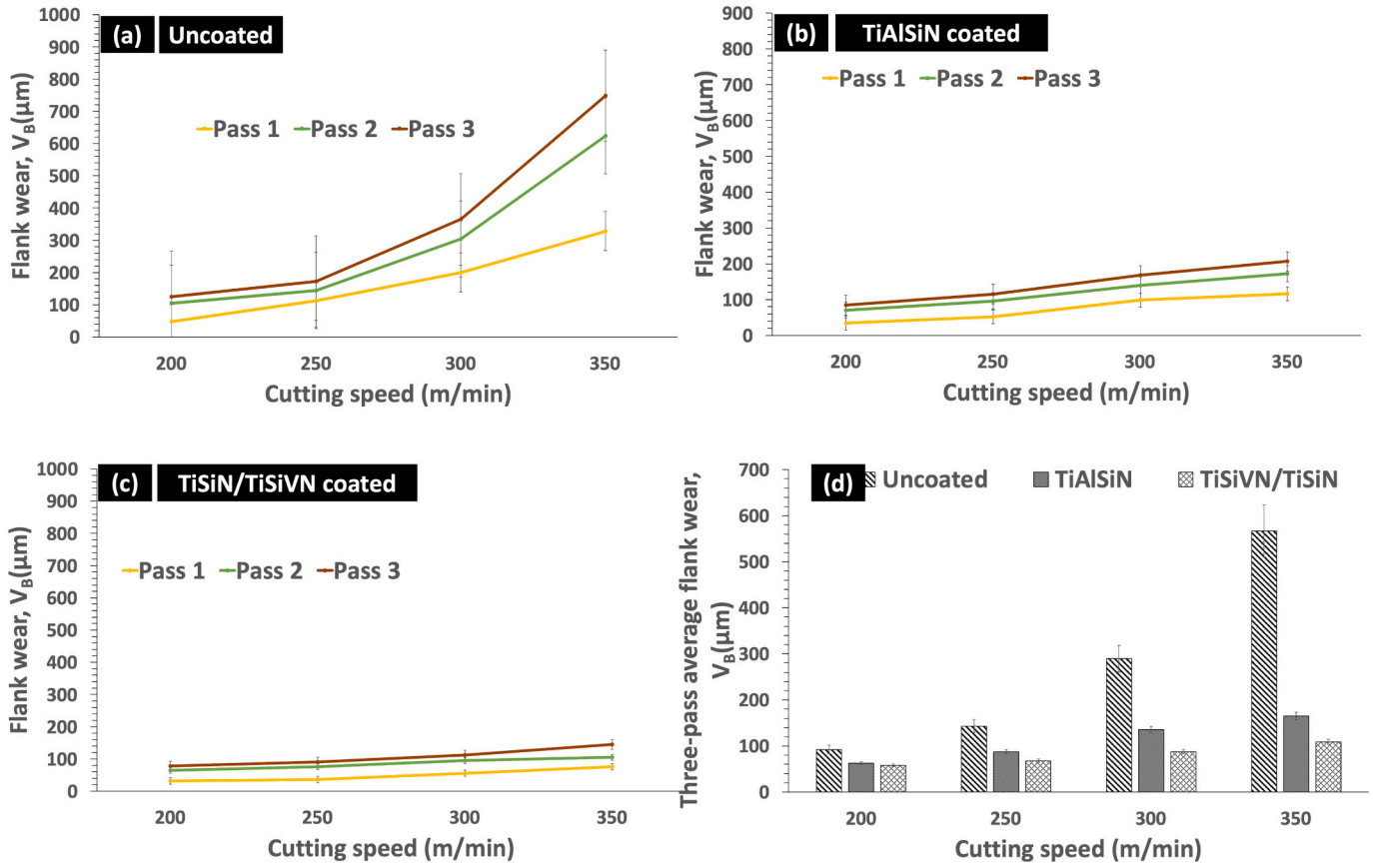

Fig. 15. Variation of flank wear V_B with cutting speed and subsequent passes for (a) Uncoated, (b) TiAlSiN coated, and (c) TiSiN/TiSiVN coated tools and (d) three-pass average flank wear variation with cutting speed for coated and uncoated cutting tools.

3.6.1. *Uncoated tool*

The SEM micrographs in Fig. 9 show severe crater formation on the rake surface of the uncoated Al_2O_3/SiC ceramic tool. The crater appears as a deep cavity in the central chip contact zone, with signs of abrasive grooves and adhesion patches surrounding it. The crater edges reveal evidence of delamination and flaking, suggesting thermal fatigue and mechanical erosion. Fig. 10 presents the EDS elemental mapping of the marked region. High concentrations of Fe, Cr, and Ni confirm the presence of adhered workpiece material. The mapping also reveals oxygen, implying oxidation of the adhered steel into Fe_2O_3 and Cr_2O_3. However, no Ti or Al oxides are detected, as expected for an uncoated ceramic substrate that lacks metallic constituents capable of forming protective tribo-oxides. These observations are consistent with previous studies on uncoated ceramics, where severe crater formation, chip welding, and oxidation-induced wear were reported during stainless steel machining [39,41,43].

3.6.2. *TiAlSiN-coated tool*

The crater wear profile on the TiAlSiN-coated tool is shown in Fig. 11. Compared to the uncoated case, the crater is notably shallower and more evenly distributed. The primary wear mechanisms appear to be abrasion and localized adhesion. The coating remains largely intact, with only minor micro-chipping near the cutting edge, and no significant coating delamination. In Fig. 12, the EDS mapping confirms the presence of Al and O near the worn area, verifying the formation of Al_2O_3. This thermally stable oxide acts as a protective tribo-layer that limits chemical reactivity at the cutting interface. Ti content is relatively low in the crater zone, suggesting preferential removal of Ti-rich phases. Moreover, the presence of Fe and Cr is limited to small isolated patches, indicating reduced adhesion of the workpiece material compared to the uncoated tool. These findings are consistent with reports on nanocomposite coatings like TiAlSiN, where Al_2O_3 formation contributes to oxidation resistance and coating integrity during dry cutting [20,42].

3.6.3. *TiSiN/TiSiVN-coated tool*

Fig. 13 presents the crater wear morphology for the TiSiN/TiSiVN multilayer-coated tool. The crater is shallow and uniform, with limited edge cracking and minimal evidence of built-up edge formation. Importantly, no significant coating spallation is observed, although fine cracking patterns are visible at higher speeds or in later passes. The EDS elemental mapping in Fig. 14 reveals the presence of vanadium and oxygen in the crater region, confirming the formation of V_2O_5. Additionally, moderate levels of Ti and Si are detected, while Fe, Cr, and Ni concentrations are minimal. This strongly suggests that the V-enriched coating resists adhesion of workpiece material and benefits from self-adaptive tribo-oxide generation during cutting. These observations are supported by studies on vanadium-based adaptive tribo-films, which highlight their lubricating effect, thermal stability, and wear control under high-speed dry machining conditions [25,40,44,45].

3.7. *Flank wear analysis*

Flank wear (V_B), which develops on the clearance face of the cutting tool, is widely regarded as a critical criterion for evaluating tool life and machining stability, especially in dry cutting environments. Progressive flank wear leads to dimensional inaccuracies, increased surface roughness, and ultimately, catastrophic tool failure. The evolution of V_B with increasing cutting speed and tool condition is illustrated in Fig. 15(a–d), while Fig. 16 presents representative SEM micrographs elucidating the dominant wear mechanisms for uncoated, TiAlSiN-coated, and TiSiN/TiSiVN-coated ceramic inserts.

The uncoated Al_2O_3/SiC composite tool exhibited the most

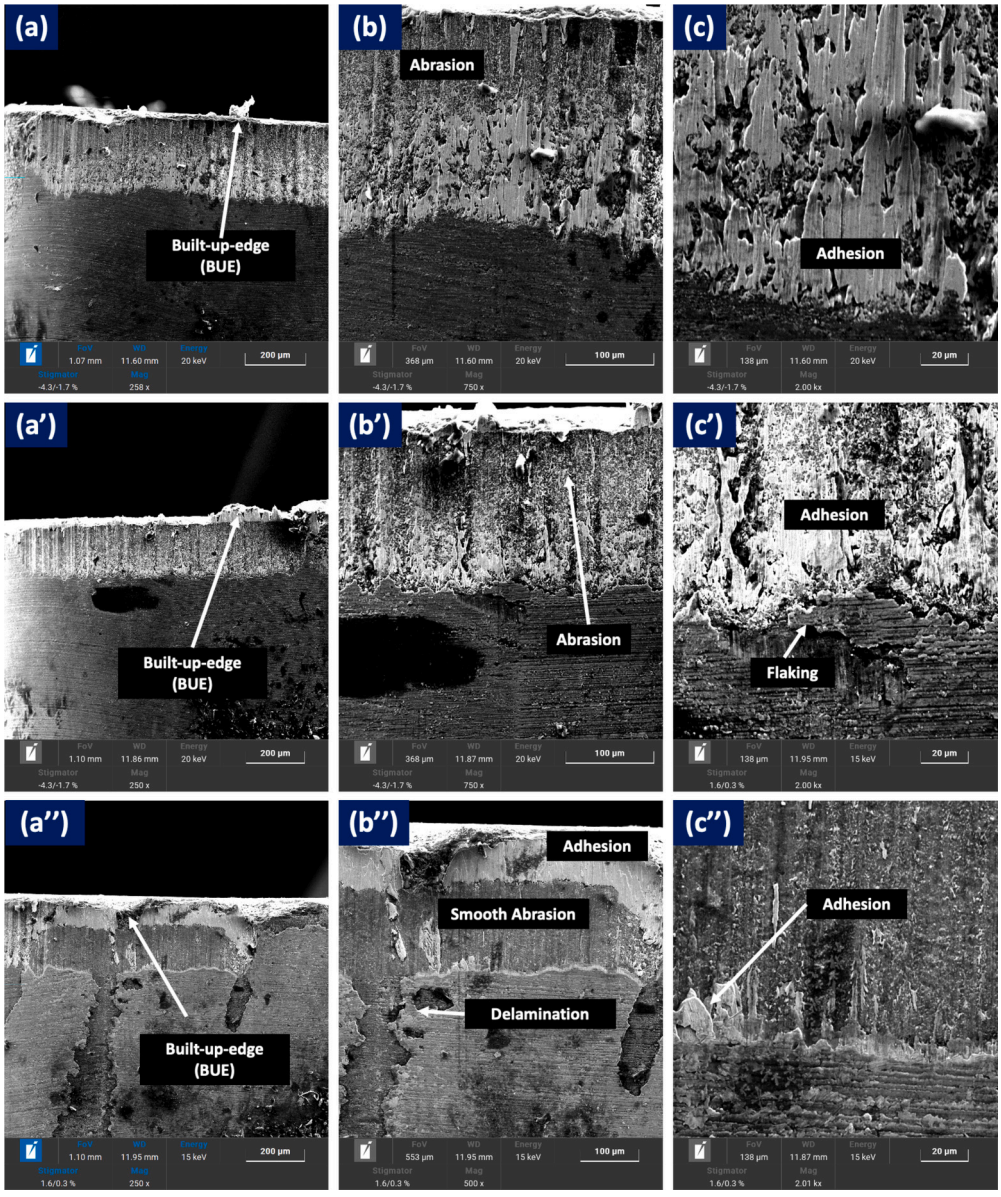

Fig. 16. SEM micrographs showing flank wear: a,b and c for uncoated tool, a', b', and c' for TiAlSiN coated tool, a'',b'' and c'' for TiSiN/TiSiVN coated tool.

Table 3
Summary of flank wear progression and mechanisms at 350 m/min.

Tool Condition	Pass 1 → 2 Increase	Pass 2 → 3 Increase	Total Wear Increase	Dominant Wear Mechanisms
Uncoated	~33 %	~36 %	~90 %+	Abrasion, adhesion, BUE formation, flaking
TiAlSiN-coated	~29 %	~25 %	~60 %	Abrasion, Al_2O_3 tribo-layer breakdown, delamination
TiSiN/TiSiVN-coated	~25 %	~17 %	~40 %	V_2O_5-based lubrication, smooth abrasion, crack deflection

aggressive wear characteristics across all cutting speeds and passes. At 200 m/min, the VB increased by approximately 33 % from Pass 1 to Pass 2, followed by a further 36 % increment from Pass 2 to Pass 3. At the elevated speed of 350 m/min, the total VB increase exceeded 90 %, indicating accelerated edge degradation under thermal and mechanical stresses. SEM analysis (Fig. 16a–c) revealed prominent abrasive grooves, substantial BUE accumulation, and extensive material transfer from the workpiece. The lack of any protective tribological layer resulted in repeated adhesion–fracture cycles and microstructural fragmentation, consistent with previous findings on uncoated ceramics under high-temperature dry cutting [39,43].

In contrast (see Table 3), the TiAlSiN-coated tool demonstrated more restrained wear progression. At 200 m/min, the flank wear increased by ~29 % between Passes 1 and 2, and by an additional ~25 % from Pass 2 to Pass 3. Even at 350 m/min, the overall VB increase remained limited to approximately 60 %, significantly lower than the uncoated counterpart. SEM micrographs (Fig. 16a'–c') displayed localized abrasion, compact BUE patches, and minor delamination near the tool edge. The enhanced performance is attributed to the formation of thermally stable Al_2O_3 tribo-oxides, which retard diffusion wear and inhibit adhesive interaction. However, under sustained thermal loads, the passive oxide layer undergoes attrition and local fracture, leading to progressive coating degradation—findings corroborated by prior evaluations of TiAlSiN-based multilayer coatings in severe machining conditions [18,42,46].

The TiSiN/TiSiVN multilayer-coated tool exhibited the most favorable wear resistance profile across the evaluated speeds. At 200 m/min,

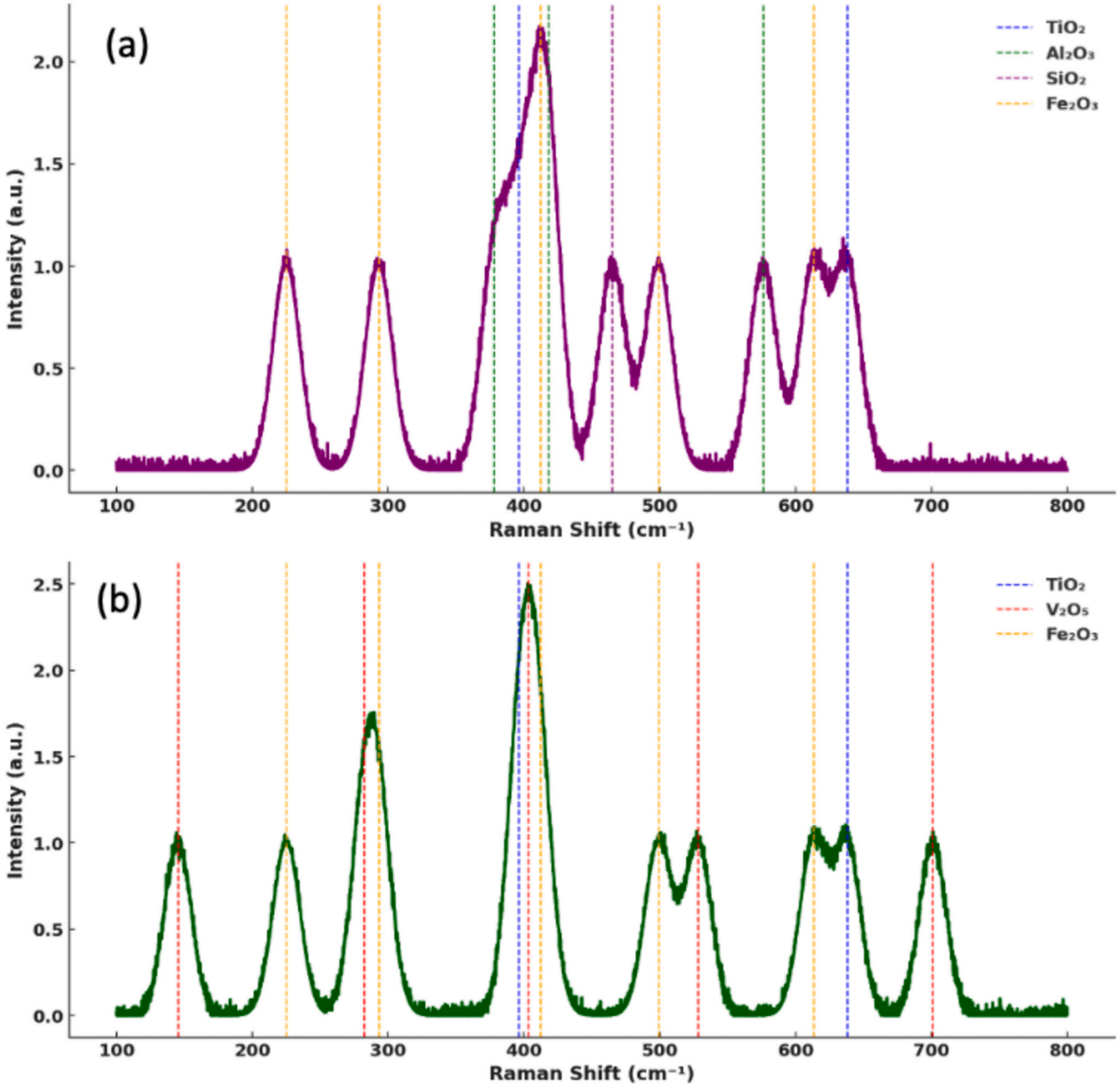

Fig. 17. Raman spectrum of chip-tool interface for (a) TiAlSiN coated tool and (b) TiSiN/TiSiVN coated tool.

Table 4
Tool performance comparison at 350 m/min (Pass 3).

Metric	Uncoated Tool	TiAlSiN-Coated Tool	TiSiN/TiSiVN-Coated Tool
Cutting Force Increase	~30 %	~25 %	~15 %
Coefficient of Friction Rise	~20 %	~15 %	~12 %
Surface Roughness (R_A)	Highest	Moderate	Lowest (~30 % improvement)
Cutting Temperature	Highest	Moderate	~20–25 % Lower
Flank Wear Increase	~90 %	~60 %	~40 %
Adhesion	Severe	Moderate	Minimal
Overall, Tool Performance	Poor	Intermediate	Superior

the increase in VB was limited to ~25 % from Pass 1 to 2, followed by a further ~17 % increase from Pass 2 to 3. Even at the maximum cutting speed of 350 m/min, the total progression in VB was confined to ~40 %, reflecting enhanced tribo-thermal stability. SEM observations (Fig. 16a″–c″) indicated smoother wear tracks, absence of large BUE zones, and the presence of continuous, low-shear tribo-films.

As observed in Fig. 15(d), the three-pass average flank wear at 350 m/min was lowest for TiSiN/TiSiVN (~40 % increase), followed by TiAlSiN (~60 %), and highest for the uncoated tool (~90 %+). These results confirm that the combined effect of adaptive tribo-film formation and stress-resistant multilayer construction makes TiSiN/TiSiVN a superior coating system for dry high-speed turning of austenitic stainless steels.

3.8. Raman analysis of chip-tool interface

Fig. 17 shows the Raman spectrum following the Raman

spectroscopic analysis so as to investigate the chemical nature of tribo-oxides formed at the chip–tool interface during dry machining of austenitic stainless steel (AISI 316 L) using TiAlSiN and TiSiN/TiSiVN coated tools. The Raman spectra of both tools exhibited characteristic bands corresponding to Fe_2O_3 [47], primarily attributed to oxidation of the workpiece material under elevated thermal conditions. However, clear distinctions in oxide phase distribution were observed between the two tool coatings. The TiAlSiN-coated tool surface revealed prominent Raman bands near 396 and 638 cm^{-1}, which are characteristic of the anatase and rutile phases of TiO_2, respectively [48]. Additional peaks around 378, 418, and 576 cm^{-1} confirm the formation of Al_2O_3 [49], while the weak band at approximately 465 cm^{-1} can be attributed to SiO_2 [50]. These oxide phases contribute to thermal stability and mild oxidation resistance but exhibit limited tribological benefits in terms of friction reduction.

Conversely, the TiSiN/TiSiVN-coated tool exhibited a more complex oxide profile. In addition to TiO_2 and SiO_2 bands, a series of distinct peaks were identified at ~145, 282, 403, 528, and 701 cm^{-1}, which are consistent with the presence of crystalline V_2O_5 [45]. The formation of V_2O_5 is particularly relevant due to its ability to form a glassy lubricating film with low shear strength at elevated temperatures. This self-lubricating oxide phase likely contributes to the lower friction and enhanced wear resistance observed during dry machining. The Raman findings underscore the superior tribological performance of TiSiN/TiSiVN coatings, where the presence of V_2O_5 not only acts as a solid lubricant but also suppresses abrasive interactions and mitigates thermal softening at the cutting edge. In contrast, TiAlSiN coatings rely primarily on thermally stable but non-lubricating oxides, resulting in comparatively higher frictional resistance.

3.9. Summary and correlation of key parameters

The interplay among cutting force, surface roughness, cutting temperature, and wear characteristics reveals a comprehensive picture of tool performance under dry turning conditions. The cutting force, primarily governed by friction at the tool–chip interface and tool edge stability, was observed to escalate with increasing speed and pass count, particularly in the uncoated tool due to the absence of protective oxides and rapid thermal degradation. In contrast, the TiSiN/TiSiVN-coated tool exhibited significantly lower force progression, a result of reduced interfacial friction. Moreover, the multilayer architecture effectively redistributes stress and deflects micro-cracks at interlayer interfaces, mitigating coating delamination and extending tool integrity under aggressive cutting conditions [51–54]. These reductions in force directly translated into improved surface finish, as smoother chip flow and less mechanical vibration resulted in lower surface roughness values, accounting for ~30 % improvement with TiSiN/TiSiVN coating. Simultaneously, cutting temperature trends mirrored the force and roughness behavior; higher forces led to elevated thermal loads in uncoated tools, promoting oxidation, edge softening, and tool wear. Conversely, the formation of adaptive oxides such as Al_2O_3 in TiAlSiN and V_2O_5 in TiSiN/TiSiVN coatings provided thermal shielding, delaying tool softening and reducing temperature rise by up to ~25 %. These thermal and mechanical advantages collectively mitigated tool wear. Flank wear, which is sensitive to cumulative thermal-mechanical stress, was most pronounced in the uncoated tool and least in the TiSiN/TiSiVN tool, with ~90 % and ~ 40 % progression, respectively, reflecting the effectiveness of multilayer crack deflection and oxide-based lubrication. Crater wear showed a similar hierarchy; deep craters and severe Fe/Cr adhesion were evident in the uncoated tool, while TiSiN/TiSiVN maintained shallow wear profiles due to minimal chip welding and robust tribo-chemical defense. Thus, the superior performance of TiSiN/TiSiVN is attributed to its synergistic control over friction, heat, and wear through multilayer reinforcement and formation of adaptive vanadium-based oxides, demonstrating a holistic advantage over TiAlSiN and uncoated counterparts. An overall comparison of all the results is made in Table 4.

4. Conclusions

1. Cutting Forces progressively increased across passes for all tools; however, TiSiN/TiSiVN exhibited the lowest rise (~15 %), due to reduced friction and crack-resistant multilayer architecture.
2. Coefficient of Friction trends correlated well with force behavior; TiSiN/TiSiVN displayed the smallest percentage increase (~12 %) owing to the lubricating effect of V_2O_5 films.
3. Surface Roughness was minimized with TiSiN/TiSiVN, with up to ~30 % lower Ra values compared to the uncoated tool, attributed to stable chip flow and minimal tool deformation.
4. Cutting Temperature was highest in uncoated tools; TiSiN/TiSiVN maintained thermal control with ~20–25 % lower temperature rise, due to oxide barrier layers.
5. Flank Wear analysis showed ~40 % progression in TiSiN/TiSiVN at 350 m/min, significantly lower than uncoated (~90 %) and TiAlSiN (~60 %), confirming superior edge retention.
6. SEM/EDS and Raman analysis revealed key oxide compositions governing wear behavior-Al_2O_3 in TiAlSiN and V_2O_5 in TiSiN/TiSiVN, providing chemical stability and thermal shielding.
7. Overall, TiSiN/TiSiVN demonstrated optimal performance across all metrics due to its adaptive self-lubricating capability.

CRediT authorship contribution statement

Ch. Sateesh Kumar: Investigation, Funding acquisition, Conceptualization. **Luis Norberto López De Lacalle:** Visualization, Project administration, Investigation, Funding acquisition, Data curation, Conceptualization. **Albano Cavaleiro:** Visualization, Data curation. **Diogo Cavaleiro:** Validation, Resources. **Mitjan Kalin:** Investigation. **Ramanand Prajapati:** Supervision. **Filipe Fernandes:** Visualization, Methodology, Conceptualization.

Declaration of competing interest

The authors declare that they have no known competing financial interests or personal relationships that could have appeared to influence the work reported in this paper.

Acknowledgement

The authors acknowledge the financial support of the Slovenian Research Agency ARIS under the Research Core Funding Program No. P2-0231 and the project MSCA-COFUND-5100-237/2023-9. This research is also supported by FEDER Funds through Portugal 2020 (PT2020), by the Competitiveness and Internationalization Operational Program (COMPETE 2020), and national funds through the Portuguese Foundation for Science and Technology (FCT) under the projects: MCTool21-ref:" POCI-01-0247-FEDER-045940", UIDB/00285/2020 and LA/P/0112/2020. Thanks are also addressed to project CPP2024-011659, TWIN5, funded by Spanish Ministry of Universities, and Basque Goverment in Excellent groups call IT1573-22.

Data availability

Data will be made available on request.

References

[1] D. Vasumathy, A. Meena, Influence of Micro Scale Textured Tools on Tribological Properties at Tool-chip Interface in Turning AISI 316 Austenitic Stainless Steel 377, 2017, pp. 1747–1758.
[2] M. Moreno, J.M. Andersson, R. M'Saoubi, V. Kryzhanivskyy, M.P. Johansson-Jöesaar, L.J.S. Johnson, M. Odén, L. Rogström, Adhesive wear of TiAlN coatings during low speed turning of stainless steel 316L, Wear (2023) 524–525, https://doi.org/10.1016/j.wear.2023.204838.

[3] H. Ding, B. Zou, X. Wang, J. Liu, L. Li, Microstructure, mechanical properties and machinability of 316L stainless steel fabricated by direct energy deposition, Int. J. Mech. Sci. 243 (2023) 108046, https://doi.org/10.1016/j.ijmecsci.2022.108046.

[4] J.C. Outeiro, A.M. Dias, J.L. Lebrun, V.P. Astakhov, Machining residual stresses in AISI 316L steel and their correlation with the cutting parameters, Mach. Sci. Technol. 6 (2002) 251–270, https://doi.org/10.1081/MST-120005959.

[5] A. Thakur, A. Mohanty, S. Gangopadhyay, K.P. Maity, Tool Wear and Chip characteristics during dry turning of Inconel 825, Procedia Mater. Sci. 5 (2014) 2169–2177, https://doi.org/10.1016/j.mspro.2014.07.422.

[6] A. Thakur, S. Gangopadhyay, A. Mohanty, Investigation on some machinability aspects of Inconel 825 during dry turning, Mater. Manuf. Process. 30 (2015) 1026–1034, https://doi.org/10.1080/10426914.2014.984216.

[7] R.P. Zeilmann, F. Fontanive, R.M. Soares, Wear Mechanisms During Dry and Wet Turning of Inconel 718 with Ceramic Tools, 2017, pp. 2705–2714, https://doi.org/10.1007/s00170-017-0329-7.

[8] S.K. Choudhury, Comparative evaluations of nose wear progression and failure modes during hard turning under dry and near-dry cutting conditions Satish Chinchanikar *, Int. J. Mach. Mach. Mater. 18 (2016) 466–482, https://doi.org/10.1504/IJMMM.2016.078991.

[9] J.S. Dureja, V.K. Gupta, V.S. Sharma, M. Dogra, Design optimization of cutting conditions and analysis of their effect on tool wear and surface roughness during hard turning of AISI-H11 steel with a coated-mixed ceramic tool, Proc. Inst. Mech. Eng. B J. Eng. Manuf. 223 (2009) 1441–1453, https://doi.org/10.1243/09544054JEM1498.

[10] W.F. Sales, L.A. Costa, S.C. Santos, A.E. Diniz, J. Bonney, E.O. Ezugwu, Performance of coated, cemented carbide, mixed-ceramic and PCBN-H tools when turning W320 steel, Int. J. Adv. Manuf. Technol. 41 (2009) 660–669, https://doi.org/10.1007/s00170-008-1523-4.

[11] S. Chinchanikar, S.K. Choudhury, Hard turning using HiPIMS-coated carbide tools: Wear behavior under dry and minimum quantity lubrication (MQL), Measurement (Lond) 55 (2014) 536–548, https://doi.org/10.1016/j.measurement.2014.06.002.

[12] A. Panda, S. Ranjan Das, D. Dhupal, Machinability investigation of HSLA steel in hard turning with coated ceramic tool: assessment, modeling, optimization and economic aspects, J. Adv. Manuf. Syst. 18 (2019) 625–655, https://doi.org/10.1142/S0219686719500331.

[13] M.Y. Noordin, V.C. Venkatesh, S. Sharif, Dry turning of tempered martensitic stainless tool steel using coated cermet and coated carbide tools, J. Mater. Process. Technol. 185 (2007) 83–90, https://doi.org/10.1016/j.jmatprotec.2006.03.137.

[14] R.T. Coelho, E.G. Ng, M.A. Elbestawi, Tool wear when turning hardened AISI 4340 with coated PCBN tools using finishing cutting conditions, Int. J. Mach. Tool Manuf. 47 (2007) 263–272, https://doi.org/10.1016/j.ijmachtools.2006.03.020.

[15] D. Yu, C. Wang, X. Cheng, F. Zhang, Microstructure and properties of TiAlSiN coatings prepared by hybrid PVD technology, Thin Solid Films 517 (2009) 4950–4955, https://doi.org/10.1016/j.tsf.2009.03.091.

[16] D. Yu, C. Wang, X. Cheng, F. Zhang, Microstructure and properties of TiAlSiN coatings prepared by hybrid PVD technology, Thin Solid Films 517 (2009) 4950–4955, https://doi.org/10.1016/j.tsf.2009.03.091.

[17] A.M. Hebbale, M.R. Ramesh, J. Petru, T.V. Chandramouli, M.S. Srinath, R. K. Shetty, A microstructural study and high-temperature oxidation behaviour of plasma sprayed NiCrAlY based composite coatings, Res. Eng. 25 (2025) 103926, https://doi.org/10.1016/j.rineng.2025.103926.

[18] C.S. Kumar, S.K. Patel, Effect of duplex nanostructured TiAlSiN/TiSiN/TiAlN-TiAlN and TiAlN-TiAlSiN/TiSiN/TiAlN coatings on the hard turning performance of Al 2 O 3 -TiCN ceramic cutting tools, Wear 418–419 (2019) 226–240, https://doi.org/10.1016/j.wear.2018.11.013.

[19] H. Çalişkan, A. Erdoğan, P. Panjan, M.S. Gök, A.C. Karaoğlanli, Micro-abrasion wear testing of multilayer nanocomposite tialsin/tisin/tialn hard coatings deposited on the aisi h11 steel, Materiali in Tehnologije 47 (2013) 563–568.

[20] Ch.S. Kumar, S.K. Patel, Performance analysis and comparative assessment of nano-composite TiAlSiN/TiSiN/TiAlN coating in hard turning of AISI 52100 steel, Surf. Coat. Technol. 335 (2018) 265–279, https://doi.org/10.1016/j.surfcoat.2017.12.048.

[21] L. Wu, L. Qiu, Y. Du, F. Zeng, Q. Lu, Z. Tan, L. Yin, L. Chen, J. Zhu, Structure and mechanical properties of PVD and CVD TiAlSiN coatings deposited on cemented carbide, Crystals (Basel) 11 (2021) 1–12, https://doi.org/10.3390/cryst11060598.

[22] M. Athmani, A. AL-Rjoub, D. Cavaleiro, A. Chala, A. Cavaleiro, F. Fernandes, Microstructural, mechanical, thermal stability and oxidation behavior of TiSiN/CrVxN multilayer coatings deposited by D.C. reactive magnetron sputtering, Surf. Coat. Technol. 405 (2021) 126593, https://doi.org/10.1016/j.surfcoat.2020.126593.

[23] J.J. Zeng, W. Liu, Y. Long, S.X. Gu, A.Q. Li, S.H. Wu, TiN and TiSiN coated Al2O3/TiCN ceramic cutting tools and their cutting performance, Wuji Cailiao Xuebao/J. Inorg. Mater. 30 (2015) 1089–1093, https://doi.org/10.15541/jim20150106.

[24] Y. Moritz, C. Saringer, M. Tkadletz, A. Stark, N. Schell, I. Letofsky-Papst, C. Czettl, M. Pohler, N. Schalk, Oxidation behavior of arc evaporated TiSiN coatings investigated by in-situ synchrotron X-ray diffraction and HR-STEM, Surf. Coat. Technol. 404 (2020) 126632, https://doi.org/10.1016/j.surfcoat.2020.126632.

[25] R. Franz, C. Mitterer, Vanadium containing self-adaptive low-friction hard coatings for high-temperature applications: a review, Surf. Coat. Technol. 228 (2013) 1–13, https://doi.org/10.1016/j.surfcoat.2013.04.034.

[26] C.S. Kumar, G. Urbikain, F. Fernandes, A.A.L. Rjoub, L.N.L. De Lacalle, Influence of V concentration in TiAlSiVN coating on self-lubrication, friction and tool wear during two-pass dry turning of austenitic steel 316 L, Tribol. Int. 193 (2024), https://doi.org/10.1016/j.triboint.2024.109355.

[27] C.S. Kumar, G. Urbikain, P.F. De Lucio, L.N.L. De Lacalle, C. Pérez-Salinas, S. Gangopadhyay, F. Fernandes, Investigating the self-lubricating properties of novel TiSiVN coating during dry turning of Ti6Al4V alloy, Wear (2023) 532–533, https://doi.org/10.1016/j.wear.2023.205095.

[28] W. Tillmann, J. Urbanczyk, A. Thewes, G. Bräuer, N.F. Lopes Dias, Effect of the TiSiN interlayer properties on the adhesion and mechanical properties of multilayered TiSiCN thin films, Surf. Coat. Technol. 478 (2024) 130467, https://doi.org/10.1016/j.surfcoat.2024.130467.

[29] M. Dašić, I. Ponomarev, T. Polcar, P. Nicolini, Tribological properties of vanadium oxides investigated with reactive molecular dynamics, Tribol. Int. 175 (2022) 107795, https://doi.org/10.1016/j.triboint.2022.107795.

[30] N. Fateh, G.A. Fontalvo, G. Gassner, C. Mitterer, The beneficial effect of high-temperature oxidation on the tribological behaviour of V and VN coatings, Tribol. Lett. 28 (2007) 1–7, https://doi.org/10.1007/s11249-007-9241-x.

[31] C.S. Kumar, G. Urbikain, L.N.L. de Lacalle, S. Gangopadhyay, F. Fernandes, Investigating the effect of novel self-lubricant TiSiVN films on topography, diffusion and oxidation phenomenon at the chip-tool interface during dry machining of Ti-6Al-4V alloy, Tribol. Int. 186 (2023), https://doi.org/10.1016/j.triboint.2023.108604.

[32] V.A.A. De Godoy, A.E. Diniz, Turning of interrupted and continuous hardened steel surfaces using ceramic and CBN cutting tools, J. Mater. Process. Technol. 211 (2011) 1014–1025, https://doi.org/10.1016/j.jmatprotec.2011.01.002.

[33] S. Koseki, K. Inoue, K. Sekiya, S. Morito, T. Ohba, H. Usuki, Wear mechanisms of PVD-coated cutting tools during continuous turning of Ti-6Al-4V alloy, Precis. Eng. 47 (2017) 434–444, https://doi.org/10.1016/j.precisioneng.2016.09.018.

[34] M. Dogra, V. Sharma, A. Sachdeva, N.M. Suri, Tool life and surface integrity issues in continuous and interrupted finish hard turning with coated carbide and CBN tools, Proc. Inst. Mech. Eng. B J. Eng. Manuf. 226 (2012) 431–444, https://doi.org/10.1177/0954405411418589.

[35] J. Qin, Y. Long, J. Zeng, S. Wu, Continuous and varied depth-of-cut turning of gray cast iron by using uncoated and TiN/Al2O3 coated silicon nitride-based ceramic tools, Ceram. Int. 40 (2014) 12245–12251, https://doi.org/10.1016/j.ceramint.2014.04.068.

[36] L. Chen, J. Paulitsch, Y. Du, P.H. Mayrhofer, Thermal stability and oxidation resistance of Ti–Al–N coatings, Surf. Coat. Technol. 206 (2012) 2954–2960, https://doi.org/10.1016/j.surfcoat.2011.12.028.

[37] L. Ji, H. Liu, C. Huang, S. Li, M. Yin, Z. Liu, J. Zhao, L. Xu, Effect of TiAlSiN gradient structure design on mechanical properties and microstructure of coatings, Surf. Coat. Technol. 496 (2025) 131617, https://doi.org/10.1016/j.surfcoat.2024.131617.

[38] F. Fernandes, S. Calderon V., P.J. Ferreira, A. Cavaleiro, J.C. Oliveira, Low peak power deposition regime in HiPIMS: deposition of hard and dense nanocomposite Ti-Si-N films by DOMS without the need of energetic bombardment, Surf. Coat. Technol. 397 (2020) 125996, https://doi.org/10.1016/j.surfcoat.2020.125996.

[39] M. Nouari, A. Ginting, Wear characteristics and performance of multi-layer CVD-coated alloyed carbide tool in dry end milling of titanium alloy, Surf. Coat. Technol. 200 (2006) 5663–5676, https://doi.org/10.1016/j.surfcoat.2005.07.063.

[40] S. Zhu, J. Cheng, Z. Qiao, J. Yang, High temperature solid-lubricating materials: a review, Tribol. Int. 133 (2019) 206–223, https://doi.org/10.1016/j.triboint.2018.12.037.

[41] A. Ginting, M. Nouari, Surface integrity of dry machined titanium alloys, Int. J. Mach. Tool Manuf. 49 (2009) 325–332, https://doi.org/10.1016/j.ijmachtools.2008.10.011.

[42] C.S. Kumar, S.K. Patel, Performance analysis and comparative assessment of nano-composite TiAlSiN/TiSiN/TiAlN coating in hard turning of AISI 52100 steel, Surf. Coat. Technol. 335 (2018) 265–279, https://doi.org/10.1016/j.surfcoat.2017.12.048.

[43] G. Bartarya, S.K. Choudhury, State of the art in hard turning, Int. J. Mach. Tool Manuf. 53 (2012) 1–14, https://doi.org/10.1016/j.ijmachtools.2011.08.019.

[44] J. Yuan, K. Yamamoto, D. Covelli, M. Tauhiduzzaman, T. Arif, I.S. Gershman, S. C. Veldhuis, G.S. Fox-Rabinovich, Tribo-films control in adaptive TiAlCrSiYN/TiAlCrN multilayer PVD coating by accelerating the initial machining conditions, Surf. Coat. Technol. 294 (2016) 54–61, https://doi.org/10.1016/j.surfcoat.2016.02.041.

[45] Q. Su, C.K. Huang, Y. Wang, Y.C. Fan, B.A. Lu, W. Lan, Y.Y. Wang, X.Q. Liu, Formation of vanadium oxides with various morphologies by chemical vapor deposition, J. Alloys Compd. 475 (2009) 518–523, https://doi.org/10.1016/j.jallcom.2008.07.078.

[46] R.M. Saoubi, M.P. Johansson, J.M. Andersson, R. M'Saoubi, M.P. Johansson, J. M. Andersson, Wear mechanisms of PVD-coated PCBN cutting tools, Wear 302 (2013) 1219–1229, https://doi.org/10.1016/j.wear.2013.01.074.

[47] S. Pattanayak, S.K. Sahoo, A.K. Sahoo, M.P. Satpathy, Microstructure, strength, and fiber texture evolutions in arc-based casting using low-carbon steel wire, J. Manuf. Process. 101 (2023) 1453–1467, https://doi.org/10.1016/j.jmapro.2023.07.032.

[48] W.F. Zhang, Y.L. He, M.S. Zhang, Z. Yin, Q. Chen, Raman scattering study on anatase TiO2 nanocrystals, J. Phys. D Appl. Phys. 33 (2000) 912–916, https://doi.org/10.1088/0022-3727/33/8/305.

[49] S. Vural, Ö. Sari, Synthesis and characterization of SDS assistant α-alumina structures and investigation of the effect of the calcination time on the morphology, Colloid Polym. Sci. 297 (2019) 107–114, https://doi.org/10.1007/s00396-018-4442-4.

[50] Z. Ma, X. Liao, G. Kong, J. Chu, Raman scattering of nanocrystalline silicon embedded in SiO2, Sci China Ser A Math Phys Astron 43 (2000) 414–420, https://doi.org/10.1007/BF02897165.

[51] F. Fernandes, J.C. Oliveira, A. Cavaleiro, Self-lubricating TiSi(V)N thin films deposited by deep oscillation magnetron sputtering (DOMS), Surf. Coat. Technol. 308 (2016) 256–263, https://doi.org/10.1016/j.surfcoat.2016.07.039.

[52] F. Fernandes, A. Loureiro, T. Polcar, A. Cavaleiro, The effect of increasing V content on the structure, mechanical properties and oxidation resistance of Ti–Si–V–N films deposited by DC reactive magnetron sputtering, Appl. Surf. Sci. 289 (2014) 114–123, https://doi.org/10.1016/j.apsusc.2013.10.117.

[53] F. Fernandes, J. Morgiel, T. Polcar, A. Cavaleiro, Oxidation and diffusion processes during annealing of TiSi(V)N films, Surf. Coat. Technol. 275 (2015) 120–126, https://doi.org/10.1016/j.surfcoat.2015.05.031.

[54] G. Urbikain, L.N. López de Lacalle, Modelling of surface roughness in inclined milling operations with circle-segment end mills, Simul. Model. Pract. Theory 84 (2018) 161–176, https://doi.org/10.1016/j.simpat.2018.02.003.